Riemannian Wavefield Extrapolation: Non-orthogonal coordinate systems

Jeff Shragge

Stanford Exploration Project, Mitchell Bldg., Department of Geophysics,

Stanford University, Stanford, CA 94305-2215

(January 12, 2007)

ABSTRACT

Riemanninan wavefield extrapolation (RWE) is a method for performing one-way wave propagation on generalized coordinate meshes. Previous RWE implementations assume that coordinate systems are comprised of either orthogonal or semi-orthogonal geometry. This supposition leads to situations where coordinate meshes suffer from problematic bunching, singularities or multivaluedness. This paper develops a procedure for avoiding these problems that poses wavefield extrapolation on smoother, but generally non-orthogonal, coordinate system meshes. This allows greater emphasis to be placed on generating smoother meshes for RWE rather than satisfying more restrictive criteria. Two analytic coordinate system examples are used to validate the non-orthogonal propagation theory. A method for eliminating singularities from coordinate systems is presented, and is used to calculate 2D and 3D Green's functions for cylindrical and near-spherical geometry. Results of benchmark testing suggest that the computational overhead associated with the RWE approach is roughly 35% greater than Cartesian-based extrapolation.

INTRODUCTION

A persistent goal of wave-equation migration research is to improve seismic imaging capabilities in complex geologic settings. Although ubiquitous velocity model uncertainty and uneven illumination can contribute greatly to image interpretation ambiguity in these contexts, extrapolation operator inaccuracy remains a significant problem. The central issues with conventional one-way wave-equation extrapolation operators are well documented: while naturally handling wavefield multipathing in the presence of lateral velocity variation, they are of limited accuracy at steep propagation angles and cannot propagate overturning waves by design (though extensions including phase-shift table lookup (Hale et al., 1992) or two-pass migration (Zhang et al., 2005) obviate some of these concerns). Propagation errors are subsequently manifest in migration images as defocused or misplaced reflectors or even by a complete absence of interpretable reflectivity. Accordingly, minimizing these deleterious effects should improve image quality and any subsequent interpretation based thereon.

One strategy for reducing extrapolation operator inaccuracy is to decompose the complete computational grid into subdomains oriented in the wave propagation direction (see, e.g., Gaussian beams (Hill, 2001), beam-waves (Brandsberg-Dahl and Etgen, 2003), coherent states (Albertin et al., 2001) or tilted Cartesian meshes (Etgen, 2002)). The key concept in each of these approaches is that a judicious choice of reference frame lowers the effective propagation angle, reducing the need for expensive extrapolation operators and enabling imaging of overturned waves. Sava and Fomel (2005) followed this approach in developing Riemannian wavefield extrapolation (RWE), a theory of one-way wavefield propagation through a generalized Riemannian space. This formulation specifies wave-equation operators appropriate for wavefield extrapolation on generalized computational meshes. One important ramification is that the user is free to specify the degree to which wave-propagation effects are incorporated into the computational mesh. However, finding the optimal trade-off between

computational mesh simplicity, how well the mesh conforms to the wavefield propagation direction, and the computational cost is not a straightforward task.

RWE was initially implemented to model high-quality Green's functions. This process involved extrapolating wavefields on a point-source coordinate mesh comprised of a suite of rays traced beforehand through a smoothed version of the migration velocity model. Hence, RWE computational meshes explicitly were asserted to exhibit ray-field characteristics: semi-orthogonal geometry with an extrapolation direction (i.e. travel-time along a ray) orthogonal to the two other axes (i.e. shooting angles) that are not necessarily mutually orthogonal. This supposition results in a wave-equation dispersion relationship for semi-orthogonal meshes that contains a number of mixed-domain fields, in addition to velocity, that encoded coordinate system geometry. In most examples, modeled Green's function estimates interpolated into the Cartesian domain are highly accurate at steep propagation angles; however, accuracy is compromised in certain situations exhibiting certain unfavorable mesh characteristics.

Semi-orthogonal geometry, though, can be an overly restrictive assertion. One problematic example occurs in coordinate system triplications (see upper panel of figure 1) that arise wherever a mesh is developed from a triplicating field of rays. This generates spatial singularities that lead to zero-division of the wavefield during extrapolation and cause infinite amplitudes. Although ray-coordinate triplications can be avoided by iterative velocity model smoothing, this less-than-ideal solution counters the goal of having a coordinate system conformal to the wavefield propagation direction. A second example of restrictive semi-orthogonal geometry is illustrated in Shragge and Sava (2005), who formulate a wave-equation migration from topography strategy that poses wavefield extrapolation directly in locally orthogonal meshes conformal to the acquisition surface. This approach successfully generates subsurface images beneath areas exhibiting longer wavelength and lower amplitude relief; however, imaging results in situations involving more rugged acquisition topography

degrade due to the grid compression/extension demanded by semi-orthogonality geometry (see lower panel of figure 1b).

In this paper, I argue that the RWE approach can be made more broadly applicable by resolving the issues related to semi-orthogonal geometry using a combination of localized computational mesh smoothing and the judicious removal of all coordinate triplication branches. In doing so, though, the asserted semi-orthogonality mesh geometry is lost, and one must propagate wavefields on non-orthogonal grids. Fortunately, a non-orthogonal extrapolation wavenumber can be isolated from the general RWE dispersion relationship. This wavenumber forms the basis for a one-way extrapolation operator that is used in the usual sense of wave-equation imaging.

A goal of this paper is to develop and implement a one-way wave-equation extrapolation operator appropriate for RWE in 3D non-orthogonal coordinates. A second goal is to specify a procedure for generating unconditionally triplication-free computational meshes. The development presented herein naturally follows that of Sava and Fomel (2005); however, I recast the theory in a more compact notation that leads to a closer analytic connection of the generalized computation geometry with the underlying Cartesian grid. The paper begins with the formulation of the 3D Riemannian acoustic wave-equation and the corresponding non-orthogonal one-way wavefield extrapolation wavenumber. Appendix A presents an overview of the required differential geometry theory, while the split-step Fourier extrapolation operator used in the examples is derived in Appendix B. Two analytic 2D non-orthogonal coordinate system examples are then provided to validate the theory. The final sections detail the procedure for generating triplication-free coordinate systems, present 2D and 3D Green's functions estimates modeled in cylindrical and near-spherical coordinates, respectively, and discuss the relative computational cost and memory overhead of the RWE method.

ACOUSTIC WAVE-EQUATION IN 3D GENERALIZED RIEMANNIAN SPACES

Specifying the acoustic wave-equation in a 3D Riemannian space requires formulating the physics of wave-propagation in a generalized coordinate system framework. By definition, generalized Riemannian coordinates are related to the underlying Cartesian mesh by unique transformations (i.e. non-triplicating and one-to-one). In this paper, I use a notation where a generalized coordinate system $\boldsymbol{\xi} = \{\xi_1, \xi_2, \xi_3\}$ is mapped to a Cartesian grid $\mathbf{x} = \{x_1, x_2, x_3\}$ through transformation $\xi_i(x_j) = f_i$. Provided these conditions are met, the acoustic wave-equation for a wavefield, $\mathcal{U}$, in a generalized Riemannian space is,

$$\nabla^2_{\boldsymbol{\xi}} \mathcal{U} = -\omega^2 s^2(\boldsymbol{\xi})\, \mathcal{U}, \tag{1}$$

where $\nabla^2_{\boldsymbol{\xi}}$ is the Laplacian operator applied in coordinates $\boldsymbol{\xi}$, ω is frequency, and s is the propagation slowness.

Correctly formulating the wave-equation in coordinate system $\boldsymbol{\xi}$ requires that Laplacian operator $\nabla^2_{\boldsymbol{\xi}}$ be specified by differential geometry relationships. (An overview of necessary differential geometry theory is provided in Appendix A.) The Laplacian operator in generalized coordinates is,

$$\nabla^2_{\boldsymbol{\xi}} \mathcal{U} = \frac{1}{\sqrt{|\mathbf{g}|}} \frac{\partial}{\partial \xi_i} \left(\sqrt{|\mathbf{g}|} g^{ij} \frac{\partial \mathcal{U}}{\partial \xi_j} \right) = \frac{1}{\sqrt{|\mathbf{g}|}} \frac{\partial}{\partial \xi_i} \left(m^{ij} \frac{\partial \mathcal{U}}{\partial \xi_j} \right), \quad i, j = 1, 2, 3, \tag{2}$$

where g^{ij} is an element of the metric tensor $\mathbf{g}$, $|\mathbf{g}|$ is the metric tensor discriminant, and $m^{ij} = \sqrt{|\mathbf{g}|} g^{ij}$ is weighted metric tensor element that enables a more compact notation. Unless otherwise stated, summation over all repeated indicies (i.e. $i, j = 1, 2, 3$) is assumed throughout this paper. Substituting equation 2 into 1 generates a Helmholtz equation appropriate for propagating waves through a 3D Riemannian space,

$$\frac{1}{\sqrt{|\mathbf{g}|}} \frac{\partial}{\partial \xi_i} \left(m^{ij} \frac{\partial \mathcal{U}}{\partial \xi_j} \right) = -\omega^2 s^2 \mathcal{U}. \tag{3}$$

The first step in developing a generalized RWE wave-equation dispersion relationship is to expand the derivative terms in equation 3 and multiply through by $\sqrt{|\mathbf{g}|}$ to obtain,

$$\frac{\partial m^{ij}}{\partial \xi_i}\frac{\partial \mathcal{U}}{\partial \xi_j} + m^{ij}\frac{\partial^2 \mathcal{U}}{\partial \xi_i \partial \xi_j} = -\sqrt{|\mathbf{g}|}\omega^2 s^2 \mathcal{U}. \tag{4}$$

The spatial derivative of the weighted metric tensor in the first term of equation 4 is written concisely using the following substitution,

$$n^j = \frac{\partial m^{ij}}{\partial \xi_i} = \frac{\partial m^{1j}}{\partial \xi_1} + \frac{\partial m^{2j}}{\partial \xi_2} + \frac{\partial m^{3j}}{\partial \xi_3}. \tag{5}$$

Fields n^j are interpreted as measures of the rates by which space expands, compresses and/or shears in the j^{th} direction and can be non-zero even for orthogonal coordinate systems. Using this substitution, equation 4 is rewritten,

$$n^j\frac{\partial \mathcal{U}}{\partial \xi_j} + m^{ij}\frac{\partial^2 \mathcal{U}}{\partial \xi_i \partial \xi_j} = -\sqrt{|\mathbf{g}|}\omega^2 s^2 \mathcal{U}. \tag{6}$$

A wave-equation dispersion relation is developed by replacing the partial differential operators acting on wavefield $\mathcal{U}$ with their Fourier domain wavenumber duals (Claerbout, 1985),

$$\left(m^{ij}k_{\xi_i} - \mathrm{i}n^j\right)k_{\xi_j} = \sqrt{|\mathbf{g}|}\omega^2 s^2, \tag{7}$$

where $\mathrm{i}k_{\xi_i}$ is the Fourier domain dual of differential operator $\frac{\partial}{\partial \xi_i}$. Note that the use of these dual operators is strictly accurate only for constant slowness functions. Situations where s spatially varies leads to a non-physical and simultaneous space-wavenumber dependence. However, this is routinely handled through various approximations that are discussed below.

Equation 7 represents the dispersion relationship required to propagate a wavefield through a generalized 3D Riemannian space. Quantity m^{ij} in the first term, $m^{ij}k_{\xi_i}k_{\xi_j}$, is a measure of the dot product between wavenumber vectors in the k_{ξ_i} and k_{ξ_j} directions (i.e. orthogonal wavenumbers will have a zero m^{ij} coefficient). Fields n^j in the second term, $\mathrm{i}n^jk_{\xi_j}$, represent a scaling of wavenum-

ber k_{ξ_j} caused by local expansion, contraction and/or shearing of the coordinate system in the jth direction.

Note that the expression in equation 7 reduces to the more familiar Cartesian expression when introducing $n^j = 0$ and $m^{ij} = \delta^{ij}$

$$k_{\xi_i} k_{\xi_i} = k_{\xi_1}^2 + k_{\xi_2}^2 + k_{\xi_3}^2 = \omega^2 s^2. \tag{8}$$

Extrapolation wavenumber isolation

Specifying a one-way extrapolation operator requires isolating one of the wavenumbers in equation 7. In this paper, I associate the extrapolation direction with coordinate ξ_3. Expanding equation 7 by evaluating indices and rearranging the result yields,

$$m^{33} k_{\xi_3}^2 + \left(2m^{13} k_{\xi_1} + 2m^{23} k_{\xi_2} - \mathrm{i} n^3\right) k_{\xi_3} = \sqrt{|\mathbf{g}|}\omega^2 s^2 + \mathrm{i}\left(n^1 k_{\xi_1} + n^2 k_{\xi_2}\right) - m^{11} k_{\xi_1}^2 - m^{22} k_{\xi_2}^2 - 2m^{12} k_{\xi_1} k_{\xi_2}. \tag{9}$$

An expression for wavenumber k_{ξ_3} is obtained through a complete-the-square transform,

$$m^{33}\left(k_{\xi_3} + \frac{\left(2m^{13}k_{\xi_1} + 2m^{23}k_{\xi_2} - \mathrm{i}n^3\right)}{2m^{33}}\right)^2 = \sqrt{|\mathbf{g}|}\omega^2 s^2 - k_{\xi_1}^2\left(m^{11} - \frac{\left(m^{13}\right)^2}{m^{33}}\right) - \tag{10}$$
$$k_{\xi_2}^2\left(m^{22} - \frac{\left(m^{23}\right)^2}{m^{33}}\right) - k_{\xi_1}k_{\xi_2}\left(2m^{12} - \frac{2m^{13}m^{23}}{m^{33}}\right) + \mathrm{i}k_{\xi_1}\left(n^1 - \frac{m^{13}n^3}{m^{33}}\right) + \mathrm{i}k_{\xi_2}\left(n^2 - \frac{m^{23}n^3}{m^{33}}\right) - \frac{(n^3)^2}{m^{33}}.$$

Isolating the contributions of wavenumber k_{ξ_3} yields,

$$k_{\xi_3} = -a_1 k_{\xi_1} - a_2 k_{\xi_2} + \mathrm{i}a_3 \pm \left[a_4^2\omega^2 - a_5^2 k_{\xi_1}^2 - a_6^2 k_{\xi_2}^2 - a_7 k_{\xi_1} k_{\xi_2} + \mathrm{i}a_8 k_{\xi_1} + \mathrm{i}a_9 k_{\xi_2} - a_{10}^2\right]^{\frac{1}{2}}, \tag{11}$$

where **a** is a vector of non-stationary coefficients given by,

$$\mathbf{a} = \left[\frac{g^{13}}{g^{33}} \quad \frac{g^{23}}{g^{33}} \quad \frac{n^3}{2m^{33}} \quad \frac{s}{\sqrt{g^{33}}} \quad \sqrt{\frac{g^{11}}{g^{33}} - \left(\frac{g^{13}}{g^{33}}\right)^2} \quad \sqrt{\frac{g^{22}}{g^{33}} - \left(\frac{g^{23}}{g^{33}}\right)^2} \quad \left[\frac{2g^{12}}{g^{33}} - \frac{2g^{13}g^{23}}{\left(g^{33}\right)^2}\right] \quad \left[\frac{n^1}{m^{33}} - \frac{m^{13}n^3}{\left(m^{33}\right)^2}\right] \quad \left[\frac{n^2}{m^{33}} - \frac{m^{23}n^3}{\left(m^{33}\right)^2}\right] \quad \frac{n^3}{m^{33}}\right]^{\mathbf{T}}. \tag{12}$$

Note that the coefficients contain mixed m^{ij} and g^{ij} terms and positive definite terms a_4, a_5, a_6 and a_{10} are squared.

The special Cartesian case is again recovered from the two equations above by substituting $n^j = 0$ and $g^{ij} = \delta^{ij}$ (for all values i and j indicies) in the coefficients of equation 12

$$k_{\xi_3} = \left[s^2\omega^2 - k_{\xi_1}^2 - k_{\xi_2}^2\right]^{\frac{1}{2}}. \tag{13}$$

The dispersion relationship specified by equations 11 and 12 contains ten coefficients that represent mixed-domain fields. Similar to Cartesian-based wavefield extrapolation through homogeneous media, a constant-coefficient Fourier-domain ($\omega - \boldsymbol{k_\xi}$) phase-shift extrapolation scheme can be developed to recursively advance a wavefield from level ξ_3 to level $\xi_3 + \Delta\xi_3$,

$$\mathcal{U}(\xi_3 + \Delta\xi_3, k_{\xi_1}, k_{\xi_2}; \omega) = \mathcal{U}(\xi_3, k_{\xi_1}, k_{\xi_2}; \omega) \mathrm{e}^{\mathrm{i}k_{\xi_3}\Delta\xi_3}. \tag{14}$$

If $\mathcal{U}$ represents a post-stack wavefield, an image $\mathcal{I}$ can be produced from the propagated wavefield through an imaging condition (Claerbout, 1985),

$$\mathcal{I}(\xi_3, \xi_1, \xi_2) = \sum_{\omega} \mathcal{U}(\xi_3, \xi_1, \xi_2; \omega). \tag{15}$$

Situations where coefficients vary across an extrapolation step, though, required additional approximations. One straightforward approach is to use a multi-coefficient split-step Fourier (SSF) method (Stoffa et al., 1990), which is detailed in Appendix B. This method uses Taylor expansions of the dispersion relation about a set of reference parameters to form a bulk phase-shift operator in the Fourier domain ($\omega - \boldsymbol{k_\xi}$). Differences between the reference and true parameters then form a correction term applied in the mixed $\omega - \boldsymbol{\xi}$ domain. In addition, the phase-shift extrapolation scheme can be extended to incorporate multiple reference media followed by interpolation similar to the phase-shift plus interpolation (PSPI) technique of Gazdag and Sguazzero (1984). All results in the following sections were generated with the combined PSPI plus SSF correction extrapolation operator.

Discussion

The accuracy of the multi-coefficient SSF approach is directly related to the degree to which coefficients in equation 12 vary across a propagation step. At a first glance, one might expect that far too many expansions are required to make a PSPI approach practical. (For example, three reference expansions for each of the ten terms would seemingly require $3^{10} = 22599$ separate wavefield extrapolations.) However, three factors combine to greatly reduce the total number of required reference coefficient sets.

First, the **a** coefficients in equation 11 are highly correlated because they are composed of similar metric tensor elements g^{ij}. Thus, the central issue is how accurately can we characterize vector coefficient fields. Fortunately, this problem is similar to the quantization problem in computer graphics: What is the fewest number of colors by which an image can be represented given a maximum allowable error? In this paper, I calculate reference coefficients using a multi-dimensional Lloyd's algorithm developed by Tang and Clapp (2006). This iterative procedure allows for variable rate quantization that represents the multi-dimensional histogram of the coefficients with the sparsest number of points within a specified error tolerance.

Second, numerous situations exists where some coefficients are zero or negligible. For example, the mixed-domain fields for a 3D weakly non-orthogonal coordinate system (i.e. $\max|\{g^{12}, g^{13}, g^{23}\}| << \max\{g^{11}, g^{22}, g^{33}\}$) within a kinematic approximation (i.e. no imaginary terms) can be accurately approximated with only four coefficients. (Appendix C details situations where additional approximations are appropriate.) Third, one may apply algorithms that locally smooth the coordinate system mesh, which reduces the spatial variability of the coefficients and allows a more reliable representation of wavenumber k_{ξ_3}.

NUMERICAL MODELING EXAMPLES

2D sheared Cartesian coordinate system

An instructive analytic coordinate system to examine is a 2D sheared Cartesian grid formed by a uniform shearing action on a 2D Cartesian mesh (see left panel of figure 2). This coordinate system is uniquely specified by one additional degree of freedom and is related to an underlying Cartesian mesh through the following transformation,

$$\begin{bmatrix} x_1 \\ \\ x_3 \end{bmatrix} = \begin{bmatrix} 1 & \cos\theta \\ \\ 0 & \sin\theta \end{bmatrix} \begin{bmatrix} \xi_1 \\ \\ \xi_3 \end{bmatrix}, \tag{16}$$

where θ is the shear angle of the coordinate system ($\theta = 90^\circ$ is Cartesian). The metric tensor of this transformation is,

$$\left[g_{ij}\right] = \begin{bmatrix} \frac{\partial x_k}{\partial \xi_1}\frac{\partial x_k}{\partial \xi_1} & \frac{\partial x_k}{\partial \xi_1}\frac{\partial x_k}{\partial \xi_3} \\ \\ \frac{\partial x_k}{\partial \xi_1}\frac{\partial x_k}{\partial \xi_3} & \frac{\partial x_k}{\partial \xi_3}\frac{\partial x_k}{\partial \xi_3} \end{bmatrix} = \begin{bmatrix} g_{11} & g_{13} \\ \\ g_{13} & g_{33} \end{bmatrix} = \begin{bmatrix} 1 & \cos\theta \\ \\ \cos\theta & 1 \end{bmatrix}, \tag{17}$$

and has a discriminant $|\mathbf{g}| = \sin^2\theta$ and an associated metric tensor g^{ij} given by,

$$\left[g^{ij}\right] = \frac{1}{\sin^2\theta} \begin{bmatrix} 1 & -\cos\theta \\ \\ -\cos\theta & 1 \end{bmatrix}. \tag{18}$$

Note that because the tensor in equation 18 is coordinate invariant, equation 6 simplifies to,

$$\nabla^2_{\boldsymbol{\xi}} \mathcal{U} = g^{ij} \frac{\partial^2 \mathcal{U}}{\partial \xi_i \partial \xi_j} = -\omega^2 s^2 \mathcal{U}, \tag{19}$$

which generates the following dispersion relation,

$$g^{ij} k_{\xi_i} k_{\xi_j} = \omega^2 s^2. \tag{20}$$

Expanding out these terms leads to an expression for wavenumber k_{ξ_3},

$$k_{\xi_3} = -\frac{g^{13}}{g^{33}} k_{\xi_1} \pm \sqrt{\frac{s^2\omega^2}{g^{33}} - \left(\frac{g^{11}}{g^{33}} - \left(\frac{g^{13}}{g^{33}}\right)^2\right) k^2_{\xi_1}}. \tag{21}$$

Substituting the values of the associated metric tensor in equation 18 into equation 21 yields,

$$k_{\xi_3} = \cos\theta \ \mathrm{k}_{\xi_1} \pm \sin\theta \sqrt{\mathrm{s}^2\omega^2 - \mathrm{k}_{\xi_1}^2}, \tag{22}$$

which is appropriate for performing RWE on the 2D sheared Cartesian coordinate system shown in left panel in figure 2.

The right panel of figure 2 shows the results of extrapolating plane waves in a Cartesian coordinate system sheared 25° from vertical. The background velocity model is 1500 m/s and the zero-offset data consist of 4 flat plane-waves at times $t = 0.2, 0.4, 0.6$ and 0.8 s. Zero-offset migration results generated by equation 15 show migrated reflectors at the expected depths of z=300, 600, 900, and 1200 m. Note that the propagation creates explainable boundary artifacts: reflections on the left are due to a truncated coordinate system and hyperbolic diffractions on the right are caused by truncated plane-waves.

Polar Ellipsoidal Coordinates

A second example is an ellipsoidal polar coordinate system (see upper left panel in figure 3) appropriate for migrating overturning plane-waves. A polar ellipsoidal coordinate system is specified by,

$$\begin{bmatrix} x_1 \\ \\ x_3 \end{bmatrix} = \begin{bmatrix} a(\xi_3)\xi_1 \cos\xi_3 \\ \\ a(\xi_3)\xi_1 \sin\xi_3 \end{bmatrix}, \tag{23}$$

where parameter coordinate ξ_1 is the radius from the center focus, ξ_3 is polar angle, and is $a = a(\xi_3)$ is a smooth function that controls coordinate system ellipticity and has curvature parameters $b = \frac{\partial a}{\partial \xi_3}$ and $c = \frac{\partial^2 a}{\partial \xi_3^2}$. The metric tensor g_{ij} for the polar ellipsoidal coordinate system defined in equation 23

is,

$$\left[g_{ij}\right] = \begin{bmatrix} a^2 & \xi_1\, a\, b \\ \xi_1\, a\, b & \xi_1^2(b^2+a^2) \end{bmatrix}, \tag{24}$$

and has a metric discriminant given by $|\mathbf{g}| = a^4\xi_1^2$. The associated and weighted associated metric tensors are given by,

$$\left[g^{ij}\right] = \begin{bmatrix} \frac{b^2+a^2}{a^4} & -\frac{b}{a^3\xi_1} \\ -\frac{b}{a^3\xi_1} & \frac{1}{a^2\xi_1^2} \end{bmatrix} \quad \text{and} \quad \left[m^{ij}\right] = \begin{bmatrix} \frac{\xi_1(b^2+a^2)}{a^2} & -\frac{b}{a} \\ -\frac{b}{a} & \frac{1}{\xi_1} \end{bmatrix}. \tag{25}$$

Tensors g^{ij} and m^{ij} are used to form the extrapolation wavenumber appropriate for one-way wavefield propagation on a 2D polar ellipsoidal mesh. However, because the computational mesh is non-stationary, we must also compute the n^i fields: $n^1 = \frac{a^2+2b^2-ac}{a^2}$ and $n^3 = 0$. Inserting these values leads to the following extrapolation wavenumber expression (see equation C-7),

$$k_{\xi_3} = \frac{\xi_1 b}{a} k_{\xi_1} \pm \sqrt{a^2\xi_1^2 s^2\omega^2 - \xi_1^2 k_{\xi_1}^2 - i k_{\xi_1}\xi_1 \left(\frac{a^2+2b^2-ac}{a^2}\right)}. \tag{26}$$

The kinematic approximation of equation 26 is given by,

$$k_{\xi_3} = \xi_1 \left[\frac{b}{a} k_{\xi_1} \pm \sqrt{a^2 s^2\omega^2 - k_{\xi_1}^2}\right], \tag{27}$$

and the orthogonal polar case (i.e. $a = 1$ and $b = 0$) yields,

$$k_{\xi_3} = \pm\xi_1 \sqrt{s^2\omega^2 - k_{\xi_1}^2}, \tag{28}$$

which is examined in Nichols (1994).

Figure 3 shows a wavefield extrapolation example for an ellipsoidal polar coordinate system in equation 23 defined by ellipticity parameter $a(\xi_3) = 1 + 0.2\,\xi_3 - 0.05\,\xi_3^2$. The upper and lower panels of figure 3 correspond to velocity/coordinate and wavefield domains, respectively. Similarly, the left and right panels represent the Cartesian and Riemannian domains. Note that wavefield interpolation

between the latter two domains is possible because of the established mapping relationships. The upper left panel shows the polar ellipsoidal coordinate system mesh overlying a linear $v(z) = 1500 + 0.35\,z$ m/s velocity function. The upper right panel presents the velocity model mapped into the RWE domain under the transformations defined in equation 23. The test data consist of ten plane-waves defined by a ray parameter $p_x = -0.5$ s/km. At greater depths the waves propagate faster and go through a turning point before propagating upward to the left. The tops of the waves, though, still travel through slower material and have not yet overturned. One interesting observation is that if a propagating plane-wave wavepath is well represented by a single ellipticity parameter $a = a(\xi_3)$, then a polar elliptical mesh can form the coordinate basis for a plane-wave migration strategy that is potentially more dynamic than tilted Cartesian coordinates.

GENERATING TRIPLICATION-FREE COORDINATE MESHES

A RWE computational mesh design challenge is finding a coordinate system that is fairly conformal to the wavefield propagation direction, but is unconditionally triplication-free. This problem is illustrated by the panels in figure 4. The top panel shows a v(z) velocity model with three Gaussian anomaly inclusions overlain by a ray-coordinate system calculated by the Huygens ray-front tracing method (Sava and Fomel, 2001). Note that the anomalies cause both mesh triplications to the left and right of the model, as well as a grid rarefaction directly beneath the shot-point.

The center panel shows a first-arrival Eikonal equation solution for the same shot-point presented in the top panel. Plotted over-top are single-valued Eikonal solution isochrons. Note that isochron generally conform to the propagation direction and can be used to construct the extrapolation steps of a RWE computational mesh. The first mesh generation step is to extract initial and final isochron surfaces from the Eikonal equation solution to form the inner and outer mesh boundaries. The mesh

domain is then enclosed by interpolating between the edges of the inner and outer bounding surfaces. The interior mesh can then be formed through bi-linear interpolation methods, such as blending functions (Liseikin, 2004; Shragge, 2006).

A corresponding triplication-free mesh is presented in the bottom panel of figure 4. The grid is regularly-spaced on the outer isochron and has a couple of dimples at the locations of removed triplications. These discontinuities have been reduced by applying a smoothing operator to the Eikonal equation solution before calculating the mesh. Importantly, smoothing does not greatly affect propagation accuracy because the coordinate system mesh forms only the skeleton on which wavefield extrapolation occurs.

2D Green's Function Generation

The third test uses RWE to model 2D Green's functions on coordinate systems constructed by the aforementioned approach. Figure 5 presents the slice of the SEG-EAGE salt velocity model chosen for the test. Importantly, the contrast between the salt body and sediment velocities causes complicated wavefield propagation including triplication and multipathing. The upper left panel shows the velocity model with an overlain coordinate system generated by meshing procedure discussed in the section above. The velocity model in the RWE domain is illustrated in the upper right panel.

The lower right panel shows the impulse response tests in the RWE domain. The impulses conform fairly well to the travel-time steps, except where they enter the salt body in the lower left of the image. The migration results mapped back to Cartesian space are shown in the lower left panel. The complicated wavefield left of the shot point advances through the salt body and subsequently refracts upward. Note also the presence of wide-angle reflections from the top-salt/sediment interface. Figure 6 presents a comparison test between two-way finite-difference, RWE and Cartesian

extrapolation. The three wavefields are fairly similar beneath and to the right of the shot-point except for a 90° phase-change associated with differences between modeling the Cartesian and finite difference point-source versus the RWE plane-wave. However, significant differences are noted to the left of the shot-point. The upper two panels contain strong reflections from the salt-sediment that are fairly well matched in location. Cartesian-based extrapolation, though, cannot propagate wavefields laterally with the same accuracy and upward at all. Hence, this energy is absent from the propagating wavefield in the lower panel. Another interesting observation is that the lower two panels have significantly higher amplitudes both in and directly below the salt due to differences in energy partitioning at the top-salt interface.

3D Point Source Coordinates

The procedure discussed above can be extended to 3D point-source coordinate systems. However, any wavefield extrapolation procedure in near-spherical coordinates must account for the apparent singularity at the poles. One approach is to rotate the poles such that the small arc-length regions are at the Earth's surface (Schneider, 1995). A second approach is to avoid sampling at the existing polar singularity (Fowler, 1995). Both solutions, though, have highly variable spatial sampling because regular spherical angle discritization leads to highly variable sampling in Cartesian space.

Another solution is to choose a discritization of the spherical surface that has a fairly uniform distribution in Cartesian domain. Herein, I use a 3D point source gridding technique based on the Winkel-Tripel cartographic projection (Bugayevskiy and Snyder, 1995). Note that the mapping of a spherical surface illustrated in figure 7 does not eliminate distortions in area, direction or distance; rather, it tries to minimize the sum of all three. The gridding equations for a Winkel-Tripel surface

are the following,

$$
\begin{aligned}
x_1 &= \xi_3(2\xi_1/\pi + 2\,w\,\alpha\cos\xi_2\sin(\xi_1/2))/2 \\
x_2 &= \xi_3(\xi_2 + 2\alpha\sin\xi_2)/2 \\
x_3 &= \sqrt{\xi_3^2 - x_1^2 - x_2^2}
\end{aligned}
\tag{29}
$$

where ξ_3 is in the radial direction, ξ_1 and ξ_2 are a latitude parallel and longitude meridian, respectively, and,

$$
\begin{aligned}
\alpha &= \cos^{-1}(\cos\xi_2\cos(\xi_1/2)) \\
w &= \begin{cases} 0, & \sin\alpha = 0 \\ (\sin\alpha)^{-1}, & \text{otherwise} \end{cases}
\end{aligned}
\tag{30}
$$

Note that the 3D grid is created by stepping outward in the radial direction ξ_3 (or equally by the Eikonal equation solution method described above).

Figure 8 presents an example of a wavefield extrapolated on 3D point source coordinate mesh. The Elf-IFP-CGG synthetic velocity model used in this example is inspired from field data observations from North Sea Block L7d. The sediments located beneath the shot point form a mostly v(z) profile, while the salt body to the right generates a more complex geologic setting. Overlain are a number of impulse responses associated with different travel times. Note that the wavefield does not exhibit azimuthal anisotropy found in 3D impulse response tests based on finite-difference splitting methods. Also, the coordinate system boundaries are restricted at steep angles, which generates boundary reflection artifacts. Overall, though, this extrapolation results demonstrates the stability of wavefield propagation on a 3D grid defined by the Winkel-Tripel spatial discritization.

IMPLEMENTATION COSTS

The introduction of additional mixed-domain coefficients into the dispersion relationship leads to both increased computation costs and memory requirements. To examine the cost overhead of the RWE approach, relative to Cartesian, the algorithm was benchmarked on the 512x512 computational grid used to generate figure 5. Tests were conducted on two codes that differed only in the phase-shift and split-step Fourier subroutines. The RWE code implemented the 2D non-orthogonal extrapolation operator in equation C-9, while the Cartesian implementation used the regular expression (i.e. $g_{33} = g_{11} = 1$ and $g_{13} = n_3 = 0$ in equation C-9).

Table 1 presents the results of the benchmark test. The most significant observation is that the RWE algorithm is roughly 35% slower than the equivalent Cartesian code. Most of the slowdown occurs in the phase-shift and SSF subroutines that are roughly 125% and 100% less efficient, respectively. Whether these costs may be reduced by implementing look-up tables remains an open question. An additional computational overhead is the time required to calculate tje geometrical factors **a** in equation 11. This cost, though, can usually be amortized over the total number of shots for stationary geometries.

A second major implementation issue is the memory required to store the non-stationary coefficients, **a**, of equation 11. Holding each additional coefficient in core requires allocating memory equivalent to an additional velocity model, which can become a limiting issue for large 3D model. In addition, the alternatives allocating memory, recalculating **a** locally each time or reading them from disk, are inefficient. An alternate approach is to consider analytic coordinate systems similar to those found in figures 2 and 3. Their main advantage is that they result in analytically defined extrapolation operators that avoid most problems associated with additional computational and memory overhead costs. Further discussion on this point, however, is beyond the scope of this paper.

CONCLUDING REMARKS

This paper extends the implementation of Riemannian wavefield extrapolation theory to 3D non-orthogonal coordinate systems. The extrapolation wavenumber decouples from the other wavenumbers enabling the use an approximate PSPI plus multi-coefficient SSF solution of the one-way wavefield extrapolation operator. Also documented is a methodology for generating computational meshes that are unconditionally triplication-free. The provided examples illustrate that wavefields can be extrapolated on non-orthogonal coordinate meshes, which opens up a range of possibilities including Riemannian plane-wave migration in elliptical polar coordinates.

ACKNOWLEDGMENTS

I acknowledge the contributions of Paul Sava and Sergey Fomel in laying the groundwork for the current theory and for ongoing RWE conversations, and I thank Biondo Biondi, Bob Clapp, Brad Artman, Paul Fowler, Tom Dickens, and Peter Traynor for enlightening discussions. The sponsors of the SEP consortium provided funding for this work.

REFERENCES

Albertin, U., D. Yingst, and H. Jaramillo, 2001, Comparing common-offset Maslov, Gaussian beam, and coherent state migrations: 71st Ann. Internat. Mtg., Soc. of Expl. Geophys., Expanded Abstracts, 913–916.

Brandsberg-Dahl, S. and J. Etgen, 2003, Beam-wave imaging: Soc. of Expl. Geophys., Expanded Abstracts, 977–980.

Bugayevskiy, L. M. and J. P. Snyder, 1995, Map projections - A Reference Manual: Taylor & Francis Inc., Philadelphia, PA.

Claerbout, J., 1985, Imaging the Earth's Interior: Stanford University.

Etgen, J., 2002, Waves, beams and Dimensions: An illuminating if incoherent view of the future of migration: Soc. of Expl. Geophys., invited presentation.

Fowler, P. J., 1995, Finite-difference solutions of the 3-D Eikonal equation in spherical coordinates: 65^{th} Annual SEG Convention, SEG Expanded Abstracts.

Gazdag, J. and P. Sguazzero, 1984, Migration of seismic data by phase-shift plus interpolation: Geophysics, **69**, 124–131.

Guggenheimer, H., 1977, Differential Geometry: Dover Publications, Inc., New York.

Hale, D., N. Hill, and J. Stefani, 1992, Imaging salt with turning seismic waves: Geophysics, **57**, 1453–1462.

Hill, N. R., 2001, Prestack Gaussian-beam depth migration: Geophysics, **66**, 1240–1250.

Liseikin, V., 2004, A Computational Differential Geometry Approach to Grid Generation: Springer-Verlag, Berlin.

Nichols, D., 1994, Imaging complex structures using band-limited Green's functions: Ph.D. thesis, Stanford University.

Sava, P. and S. Fomel, 2001, 3-D traveltime computation using Huygens wavefront tracing: Geophysics, **66**, 883–889.

Sava, P. and S. Fomel, 2005, Riemannian wavefield extrapolation: Geophysics, **70**, T45–T56.

Schneider, W. A., 1995, Robust and efficient upwind finite-difference traveltime calculations in three dimensions: Geophysics, **60**, 1108–1117.

Shragge, J. and P. Sava, 2005, Wave-equation migration from topography: Soc. of Expl. Geophys., Expanded Abstracts, 1842–1845.

Shragge, J., 2006, Differential mesh generation: Soc. of Expl. Geophys., Expanded Abstracts, 2206–2209.

Stoffa, P. L., J. T. Fokkema, R. M. de Luna Freire, and W. P. Kessinger, 1990, Split-step Fourier migration: Geophysics, **55**, 410–421.

Tang, Y. and R. Clapp, 2006, Selection of reference-anisotropy parameters for wavefield extrapolation by lloyd's algorithm: Soc. of Expl. Geophys., Expanded Abstracts, 189–192.

Zhang, Y., G. Zhang, and N. Bleistein, 2005, Theory of true-amplitude one-way wave equations and true-amplitude common-shot migration: Geophysics, **70**, E3–E10.

APPENDIX A

Geometry in a generalized 3D Riemannian space is described by a symmetric metric tensor, $g_{ij} = g_{ji}$, that relates the geometry in a general non-orthogonal coordinate system, $\{\xi_1, \xi_2, \xi_3\}$, to an underlying Cartesian mesh, $\{x_1, x_2, x_3\}$ (Guggenheimer, 1977). In matrix form, the metric tensor is written,

$$\left[g_{ij}\right] = \begin{bmatrix} g_{11} & g_{12} & g_{13} \\ g_{21} & g_{22} & g_{23} \\ g_{31} & g_{32} & g_{33} \end{bmatrix} = \begin{bmatrix} g_{11} & g_{12} & g_{13} \\ g_{12} & g_{22} & g_{23} \\ g_{13} & g_{23} & g_{33} \end{bmatrix}, \tag{A-1}$$

where g_{11}, g_{12}, g_{22}, g_{13}, g_{23} and g_{33} are functions linking the two coordinate systems through,

$$\begin{aligned} g_{11} &= \frac{\partial x_k}{\partial \xi_1}\frac{\partial x_k}{\partial \xi_1}, \quad g_{12} = \frac{\partial x_k}{\partial \xi_1}\frac{\partial x_k}{\partial \xi_2}, \quad g_{22} = \frac{\partial x_k}{\partial \xi_2}\frac{\partial x_k}{\partial \xi_2}, \\ g_{13} &= \frac{\partial x_k}{\partial \xi_1}\frac{\partial x_k}{\partial \xi_3}, \quad g_{23} = \frac{\partial x_k}{\partial \xi_2}\frac{\partial x_k}{\partial \xi_3}, \quad g_{33} = \frac{\partial x_k}{\partial \xi_3}\frac{\partial x_k}{\partial \xi_3}. \end{aligned} \tag{A-2}$$

The associated (or inverse) metric tensor, g^{ij}, is defined by $g_{ij} = |\mathbf{g}|\, g^{ij}$, where $|\mathbf{g}|$ is metric tensor matrix discriminant. The associated metric tensor is given by,

$$\left[g^{ij}\right] = \frac{1}{|\mathbf{g}|}\begin{bmatrix} g_{22}g_{33} - g_{23}^2 & g_{13}g_{23} - g_{12}g_{33} & g_{12}g_{23} - g_{13}g_{22} \\ g_{13}g_{23} - g_{12}g_{33} & g_{11}g_{33} - g_{13}^2 & g_{12}g_{13} - g_{11}g_{23} \\ g_{12}g_{23} - g_{13}g_{22} & g_{12}g_{13} - g_{11}g_{23} & g_{11}g_{22} - g_{12}^2 \end{bmatrix}, \tag{A-3}$$

and has the following metric discriminant,

$$|\mathbf{g}| = g_{33}(g_{11}g_{22} - g_{12}^2)\left[1 - \frac{g_{11}g_{23}^2 + g_{22}g_{13}^2 - 2g_{12}g_{23}g_{13}}{g_{33}(g_{11}g_{22} - g_{12}^2)}\right]. \tag{A-4}$$

A weighted metric tensor, $m^{ij} = \sqrt{|\mathbf{g}|}\, g^{ij}$, is also used throughout the paper.

APPENDIX B

The extrapolation wavenumber defined in equations 11 and 12 cannot generally be implemented exactly in the Fourier domain due to a simultaneous spatial dependence (i.e. a function of both x_1 and k_{ξ_1}). This can be addressed using an multi-coefficient version of the split-step Fourier approximation (Stoffa et al., 1990) that uses Taylor expansions to separate k_{ξ_3} into two parts: $k_{\xi_3} \approx k_{\xi_3}^{PS} + k_{\xi_3}^{SSF}$. Wavenumbers $k_{\xi_3}^{PS}$ and $k_{\xi_3}^{SSF}$ represent a pure Fourier $(\omega - \mathbf{k_x})$ domain phase-shift and a mixed $(\omega - \mathbf{x})$ domain split-step correction, respectively.

The phase-shift term is given by,

$$k_{\xi_3}^{PS} = -b_1 k_{\xi_1} - b_2 k_{\xi_2} + i\, b_3 \pm \left[b_4^2 \omega^2 - b_5^2 k_{\xi_1}^2 - b_6^2 k_{\xi_2}^2 - b_7 k_{\xi_1} k_{\xi_2} + b_8 i\, k_{\xi_1} + b_9 i\, k_{\xi_2} - b_{10}^2 \right]^{\frac{1}{2}}, \quad \text{(B-1)}$$

where $b_i = b_i(\xi_3)$ are reference values of $a_i = a_i(\xi_1, \xi_2, \xi_3)$. The split-step approximation is developed by performing a Taylor expansion about each coefficient a_i and evaluating the results at stationary reference values b_i. Assuming that the stationary values of k_{ξ_1} and k_{ξ_2} are zero, the split-step correction is as follows,

$$k_{\xi_3}^{SSF} = \left.\frac{\partial k_{\xi_3}}{\partial a_3}\right|_0 (a_3 - b_3) + \left.\frac{\partial k_{\xi_3}}{\partial a_4}\right|_0 (a_4 - b_4) + \left.\frac{\partial k_{\xi_3}}{\partial a_{10}}\right|_0 (a_{10} - b_{10}), \quad \text{(B-2)}$$

where "0" denotes "with respect to a reference medium". The partial differential expressions in equation B-2 are,

$$\left.\frac{\partial k_{\xi_3}}{\partial a_3}\right|_0 = b_3, \quad \left.\frac{\partial k_{\xi_3}}{\partial a_4}\right|_0 = \frac{b_4\, \omega^2}{\sqrt{b_4^2 \omega^2 - b_{10}^2}}, \quad \left.\frac{\partial k_{\xi_3}}{\partial a_{10}}\right|_0 = -\frac{b_{10}}{\sqrt{b_{10}^2 \omega^2 - b_{10}^2}}, \quad \text{(B-3)}$$

resulting in the following split-step Fourier correction wavenumber,

$$k_{\xi_3}^{SSF} = i\, b_3\, (a_3 - b_3) + \frac{b_4\, \omega^2\, (a_4 - b_4)}{\sqrt{b_4^2 \omega^2 - b_{10}^2}} - \frac{b_{10}\, (a_{10} - b_{10})}{\sqrt{b_4\, \omega^2 - b_{10}^2}}. \quad \text{(B-4)}$$

APPENDIX C

The extrapolation wavenumber developed in equation 11 is appropriate for any non-orthogonal Riemannian geometry. However, there are a number of situations where symmetry or partial orthogonality are present. Moreover, one may wish to make a kinematic approximation where all of the imaginary components of the wavenumber are ignored. These situations are discussed in this Appendix.

3D Semi-orthogonal Coordinate Systems - Semi-orthogonal coordinate systems occur where one coordinate (ξ_3) is orthogonal to the other two coordinates (ξ_1 and ξ_2) (Sava and Fomel, 2005). In these cases the m^{13} and m^{23} components of the weighted metric tensor are identically zero, which leads to the following extrapolation wavenumber,

$$k_{\xi_3} = i a_3 \pm \left[a_4^2\omega^2 - a_5^2 k_{\xi_1}^2 - a_6^2 k_{\xi_2}^2 - a_7 k_{\xi_1} k_{\xi_2} + i a_8 k_{\xi_1} + i a_9 k_{\xi_2} - a_{10}^2\right]^{\frac{1}{2}}, \tag{C-1}$$

where,

$$\mathbf{a} = \left[0 \quad 0 \quad \frac{n^3}{2m^{33}} \quad \frac{s}{\sqrt{g^{33}}} \quad \sqrt{\frac{g^{11}}{g^{33}}} \quad \sqrt{\frac{g^{22}}{g^{33}}} \quad \frac{2g^{12}}{g^{33}} \quad \frac{n^1}{m^{33}} \quad \frac{n^2}{m^{33}} \quad \frac{n^3}{m^{33}}\right]^{\mathbf{T}}. \tag{C-2}$$

which are identical to the coefficients recovered by Sava and Fomel (2005).

3D Kinematic Coordinate Systems - Wave-equation migration amplitudes are generally inexact in laterally variant media - even in Cartesian-based systems. Hence, one beneficial approximation that reduces computational cost is to consider only the kinematic terms in equation 11. This approximate generates the following extrapolation wavenumber,

$$k_{\xi_3} = -a_1 k_{\xi_1} + -a_2 k_{\xi_2} \pm \left[a_4^2\omega^2 - a_5^2 k_{\xi_1}^2 - a_6^2 k_{\xi_2}^2 - a_7 k_{\xi_1} k_{\xi_2} - a_{10}^2\right]^{\frac{1}{2}}, \tag{C-3}$$

where,

$$\mathbf{a} = \left[-\frac{g^{13}}{g^{33}} \quad -\frac{g^{23}}{g^{33}} \quad 0 \quad \frac{s}{\sqrt{g^{33}}} \quad \sqrt{\frac{g^{11}}{g^{33}} - \left(\frac{g^{13}}{g^{33}}\right)^2} \quad \sqrt{\frac{g^{22}}{g^{33}} - \left(\frac{g^{23}}{g^{33}}\right)^2} \quad \frac{2\,g^{12}}{g^{33}} - \frac{2\,g^{13}g^{23}}{\left(g^{33}\right)^2} \quad 0 \quad 0 \quad \frac{n^3}{m^{33}} \right]^{\mathbf{T}}. \tag{C-4}$$

3D Kinematic Semi-orthogonal coordinate systems - Combining the two above restrictions yields the following extrapolation wavenumber,

$$k_{\xi_3} = \pm\left[a_4^2\omega^2 - a_5^2 k_{\xi_1}^2 - a_6^2 k_{\xi_2}^2 - a_7 k_{\xi_1} k_{\xi_2} - a_{10}^2\right]^{\frac{1}{2}}, \tag{C-5}$$

where,

$$\mathbf{a} = \left[0 \quad 0 \quad 0 \quad \frac{s}{\sqrt{g^{33}}} \quad \sqrt{\frac{g^{11}}{g^{33}}} \quad \sqrt{\frac{g^{22}}{g^{33}}} \quad \frac{2\,g^{12}}{g^{33}} \; ; \; 0 \quad 0 \quad \frac{n^3}{m^{33}} \right]^{\mathbf{T}}. \tag{C-6}$$

2D Non-orthogonal coordinate systems - Two-dimensional situations are handled by identifying $\xi_2 = 0$. All derivatives in the associated metric tensor g^{ij} with respect coordinate ξ_2 are identically zero, and the resulting 2D non-orthogonal coordinate system wavenumber is,

$$k_{\xi_3} = -a_1 k_{\xi_1} + i a_3 \pm \left[a_4^2\omega^2 - a_5^2 k_{\xi_1}^2 + i a_8 k_{\xi_1} - a_{10}^2\right]^{\frac{1}{2}}, \tag{C-7}$$

where,

$$\mathbf{a} = \left[-\frac{g^{13}}{g^{33}} \quad 0 \quad \frac{n^3}{2m^{33}} \quad \frac{s}{\sqrt{g^{33}}} \quad \sqrt{\frac{g^{11}}{g^{33}} - \left(\frac{g^{13}}{g^{33}}\right)^2} \quad 0 \quad 0 \quad \frac{n^1}{m^{33}} \quad 0 \quad \frac{n^3}{m^{33}} \right]^{\mathbf{T}}. \tag{C-8}$$

2D Non-orthogonal Kinematic Coordinate Systems - Two-dimensional kinematic situations are handled through identity $\xi_2 = 0$. Again, all derivatives in the associated metric tensor g^{ij} with respect coordinate ξ_2 are identically zero, and the 2D non-orthogonal kinematic extrapolation wavenumber is

$$k_{\xi_3} = -a_1 k_{\xi_1} \pm \left[a_4^2\omega^2 - a_5^2 k_{\xi_1}^2 - a_{10}^2\right]^{\frac{1}{2}}, \tag{C-9}$$

where,

$$\mathbf{a} = \left[-\frac{g^{13}}{g^{33}} \;\; 0 \;\; 0 \;\; \frac{s}{\sqrt{g^{33}}} \;\; \sqrt{\frac{g^{11}}{g^{33}} - \left(\frac{g^{13}}{g^{33}}\right)^2} \;\; 0 \;\; 0 \;\; 0 \;\; 0 \;\; \frac{n^3}{m^{33}} \right]^{\mathbf{T}}. \tag{C-10}$$

2D Orthogonal Coordinate Systems - Two-dimensional situations are handled with $\xi_2 = g_{13} = 0$. Accordingly, all derivatives in the associated metric tensor g^{ij} with respect coordinate ξ_2 are identically zero, and the 2D non-orthogonal coordinate system is represented by

$$k_{\xi_3} = i a_3 \pm \left[a_4^2 \omega^2 - a_5^2 k_{\xi_1}^2 + i a_8 k_{\xi_1} - a_{10}^2 \right]^{\frac{1}{2}}, \tag{C-11}$$

where,

$$\mathbf{a} = \left[0 \;\; 0 \;\; \frac{n_3}{2m^{33}} \;\; \frac{s}{\sqrt{g^{33}}} \;\; \sqrt{\frac{g^{11}}{g^{33}}} \;\; 0 \;\; 0 \;\; \frac{n^1}{m^{33}} \;\; 0 \;\; \frac{n^3}{m^{33}} \right]^{\mathbf{T}}. \tag{C-12}$$

2D Orthogonal Kinematic Coordinate Systems - The above two approximations can be combined to yield the following extrapolation wavenumber for 2D orthogonal kinematic coordinate systems,

$$k_{\xi_3} = \pm \left[a_4^2 \omega^2 - a_5^2 k_{\xi_1}^2 - a_{10}^2 \right]^{\frac{1}{2}}, \tag{C-13}$$

where,

$$\mathbf{a} = \left[0 \;\; 0 \;\; 0 \;\; \frac{s}{\sqrt{g^{33}}} \;\; \sqrt{\frac{g^{11}}{g^{33}}} \;\; 0 \;\; 0 \;\; 0 \;\; 0 \;\; \frac{n^3}{m^{33}} \right]^{\mathbf{T}}. \tag{C-14}$$

Extrapolation Type	Operation	Number of Calls	Total Time (s)	Time per Frequency (s)
RWE	Frequency Loop	82	55.4	0.676
RWE	Split-step Fourier	41092	4.2	0.051
RWE	Phase-shift	112996	17.1	0.209
RWE	Interpolation	112996	4.6	0.056
Cart	Frequency Loop	82	40.9	0.499
Cart	Split-step Fourier	41092	2.1	0.026
Cart	Phase-shift	112996	7.6	0.093
Cart	Interpolation	112996	4.4	0.054

Table 1.

LIST OF TABLES

LIST OF FIGURES

difference; middle panel: Riemannian wavefield extrapolation; and bottom panel: Cartesian wavefield extrapolation. Note the fairly similar top-salt reflections in upper left of the top two panels. The lower two panels also have stronger amplitudes for the intra-salt phases.

7 Starting surface for Winkel-Tripel projection of unit hemisphere. Note that the cells on the unit hemisphere surface have nearly consistent area indicating fairly uniform sampling, and that not all parts of the unit hemisphere are sampled with this approach.

8 3D modeling test of Winkel-Tripel coordinate system using the Elf-IFP-CGG synthetic velocity. Eight wavefield snapshots are shown in the image. Note the lack of azimuthal anisotropy commonly found in 3D impulse response tests based on finite-difference splitting methods. Artifacts from boundary reflections, though, are still present throughout the volume.

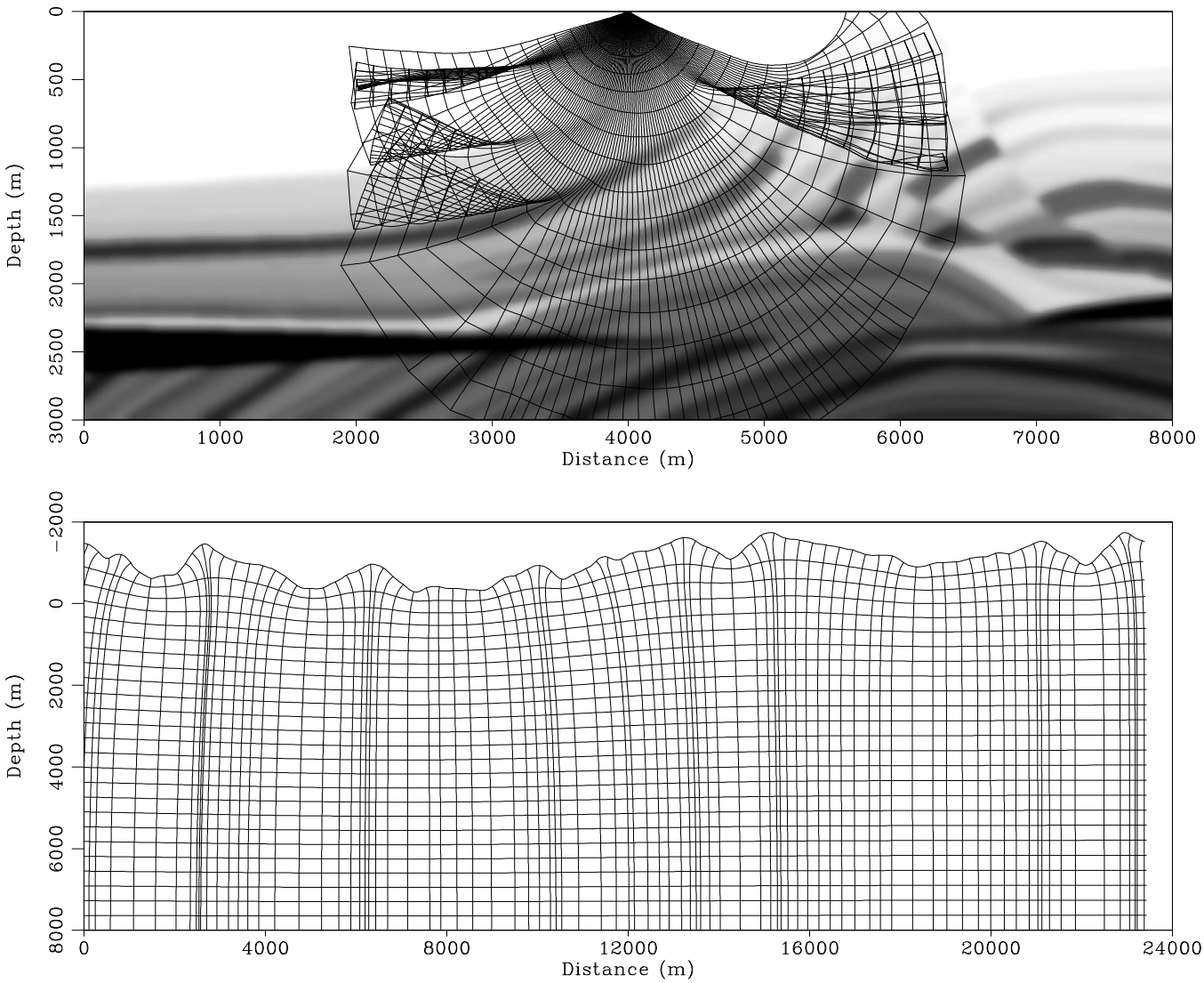
Depth (m)
0
500
1000
1500
2000
2500
3000
0
1000
2000
3000
4000
5000
6000
7000
8000
Distance (m)
Depth (m)
−2000
0
2000
4000
6000
8000
0
4000
8000
12000
16000
20000
24000
Distance (m)

Figure 1.

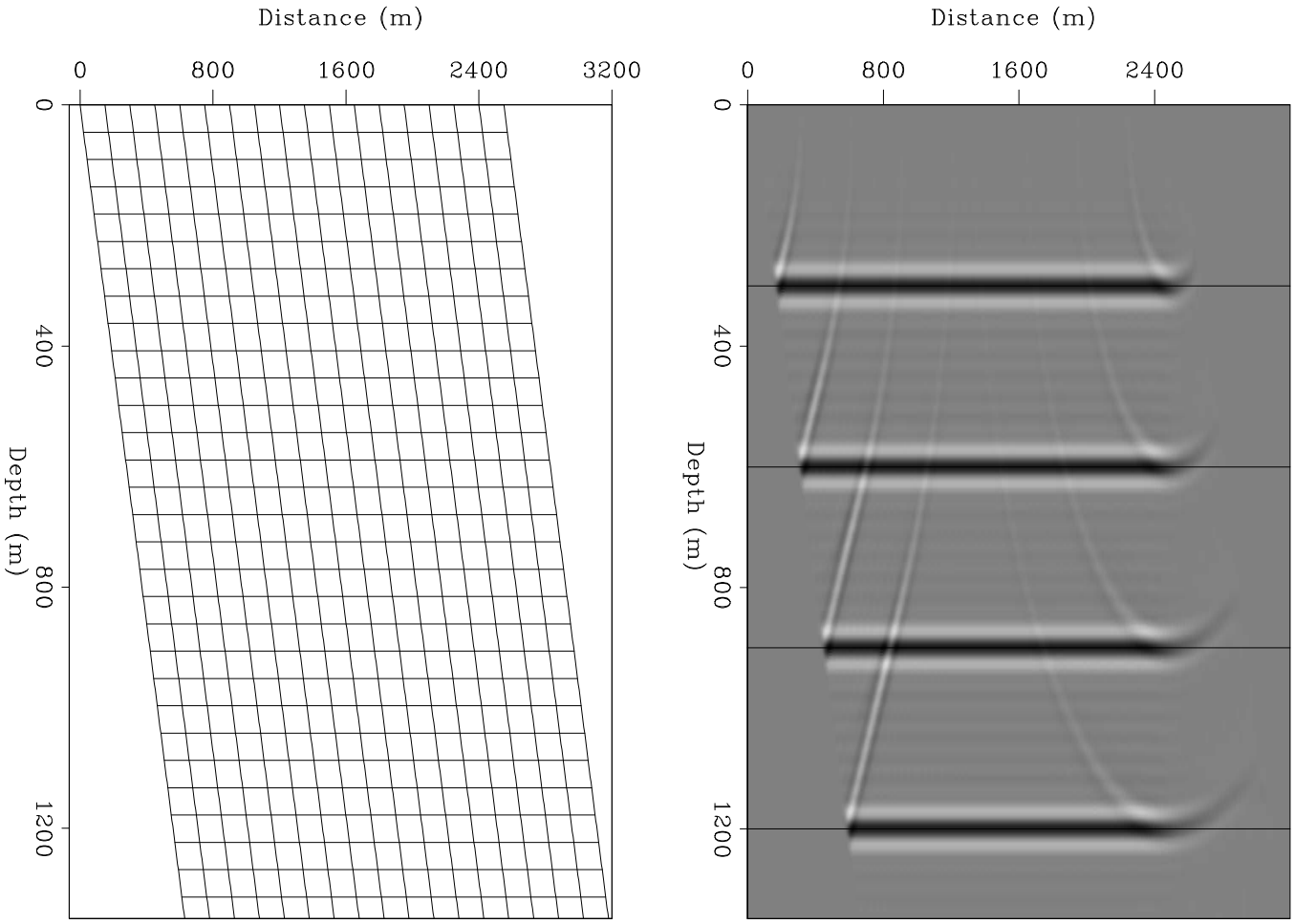
Distance (m)
0
800
1600
2400
3200
Depth (m)
0
400
800
1200
Distance (m)
0
800
1600
2400
Depth (m)
0
400
800
1200

Figure 2.

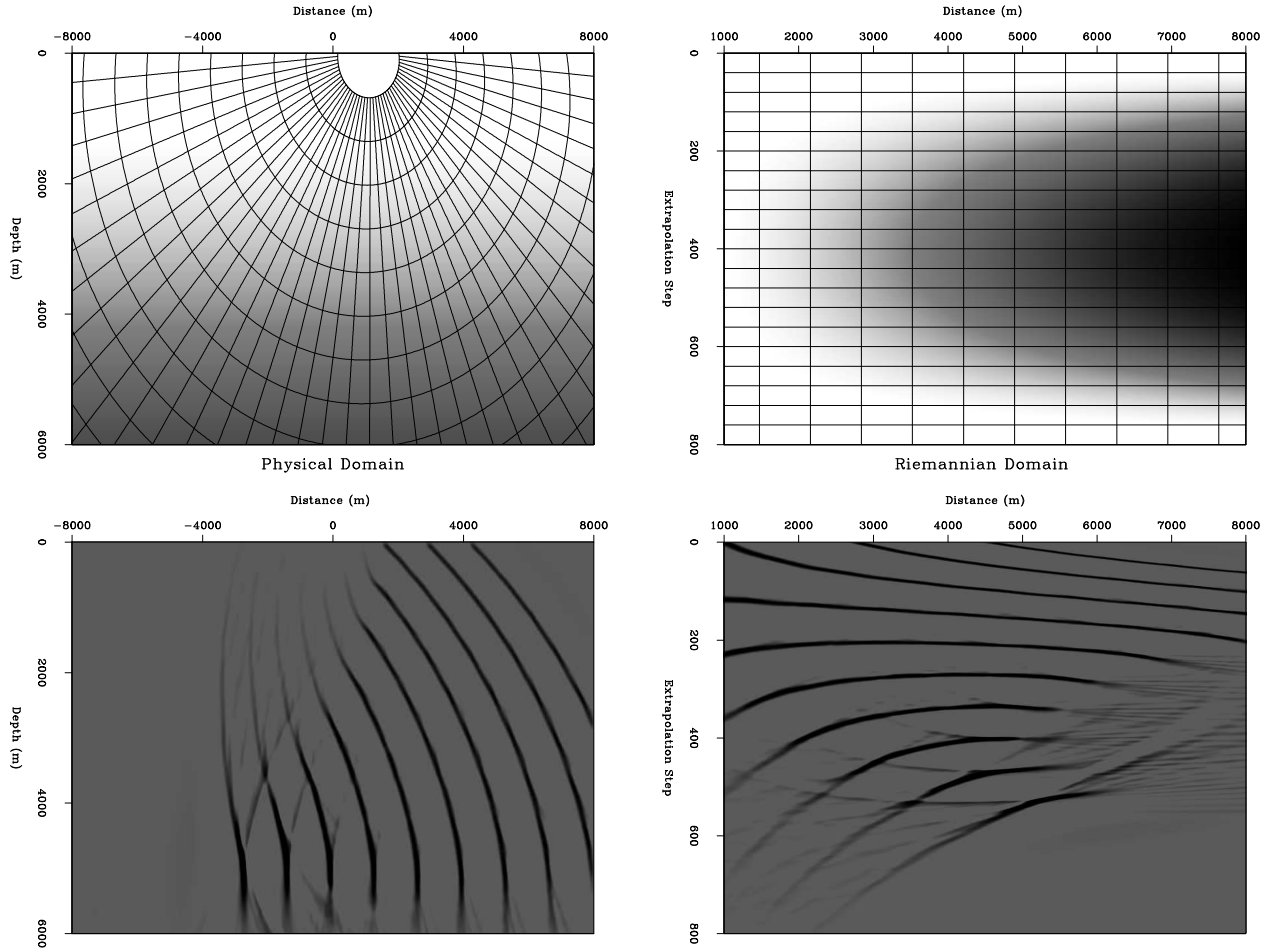
Distance (m)
−8000
−4000
0
4000
8000
Depth (m)
0
2000
4000
6000
Physical Domain
Distance (m)
1000
2000
3000
4000
5000
6000
7000
8000
Extrapolation Step
0
200
400
600
800
Riemannian Domain
Distance (m)
−8000
−4000
0
4000
8000
Depth (m)
0
2000
4000
6000
Distance (m)
1000
2000
3000
4000
5000
6000
7000
8000
Extrapolation Step
0
200
400
600
800

Figure 3.

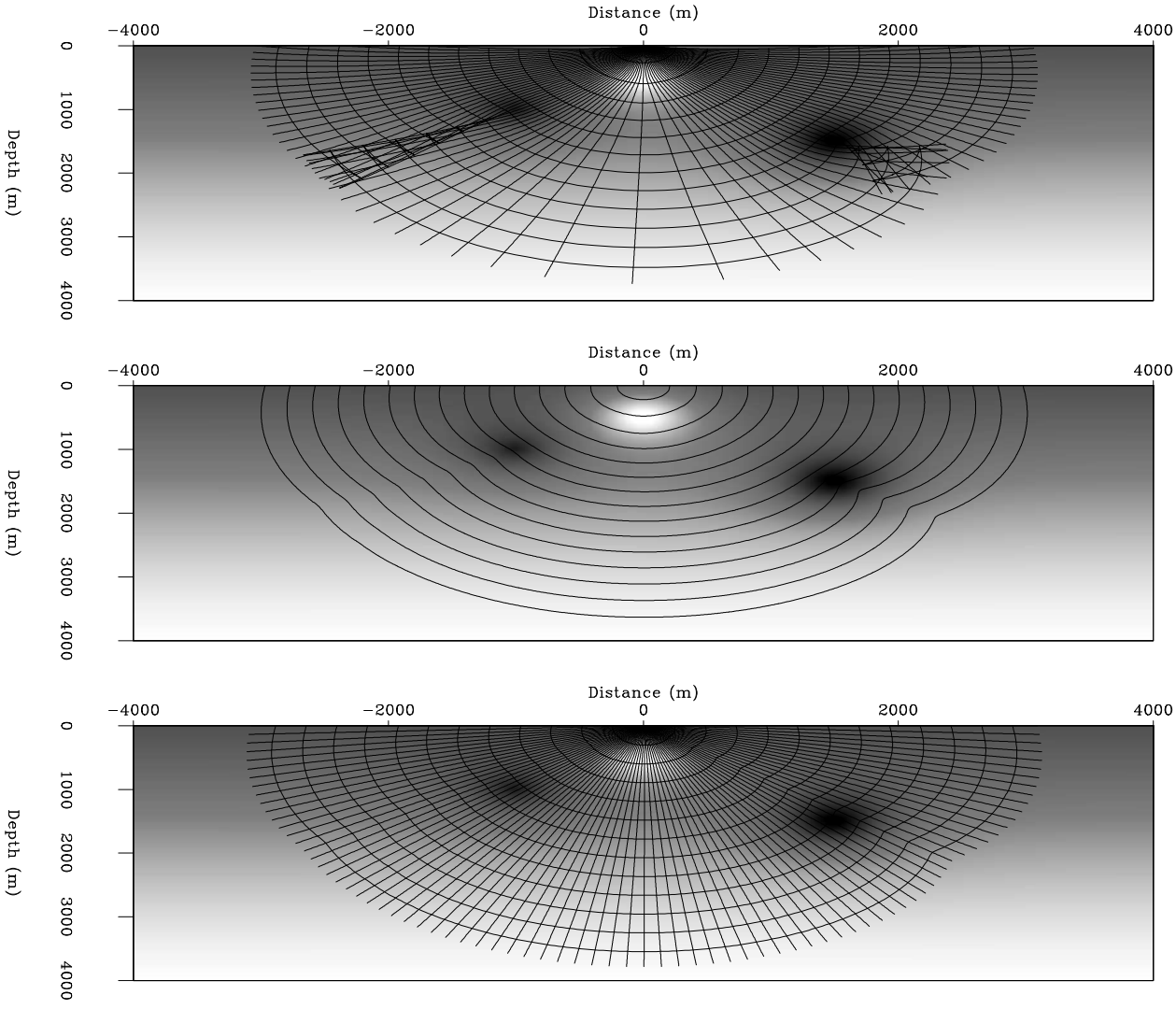
Distance (m)
−4000
−2000
0
2000
4000
Depth (m)
0
1000
2000
3000
4000
Distance (m)
−4000
−2000
0
2000
4000
Depth (m)
0
1000
2000
3000
4000
Distance (m)
−4000
−2000
0
2000
4000
Depth (m)
0
1000
2000
3000
4000

Figure 4.

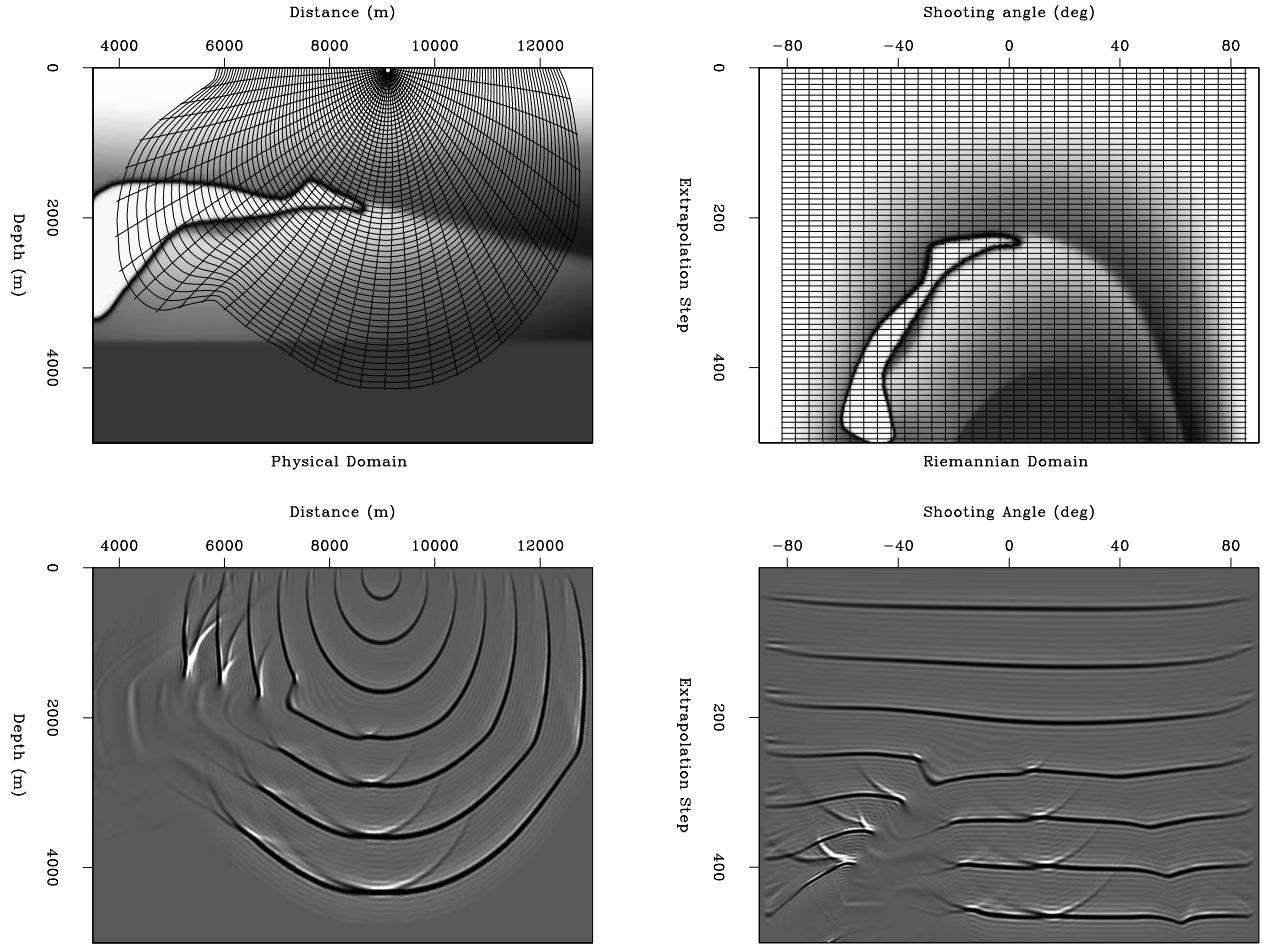
Distance (m)
4000
6000
8000
10000
12000
0
2000
4000
Depth (m)
Physical Domain
Shooting angle (deg)
−80
−40
0
40
80
0
200
400
Extrapolation Step
Riemannian Domain
Distance (m)
4000
6000
8000
10000
12000
0
2000
4000
Depth (m)
Shooting Angle (deg)
−80
−40
0
40
80
0
200
400
Extrapolation Step

Figure 5.

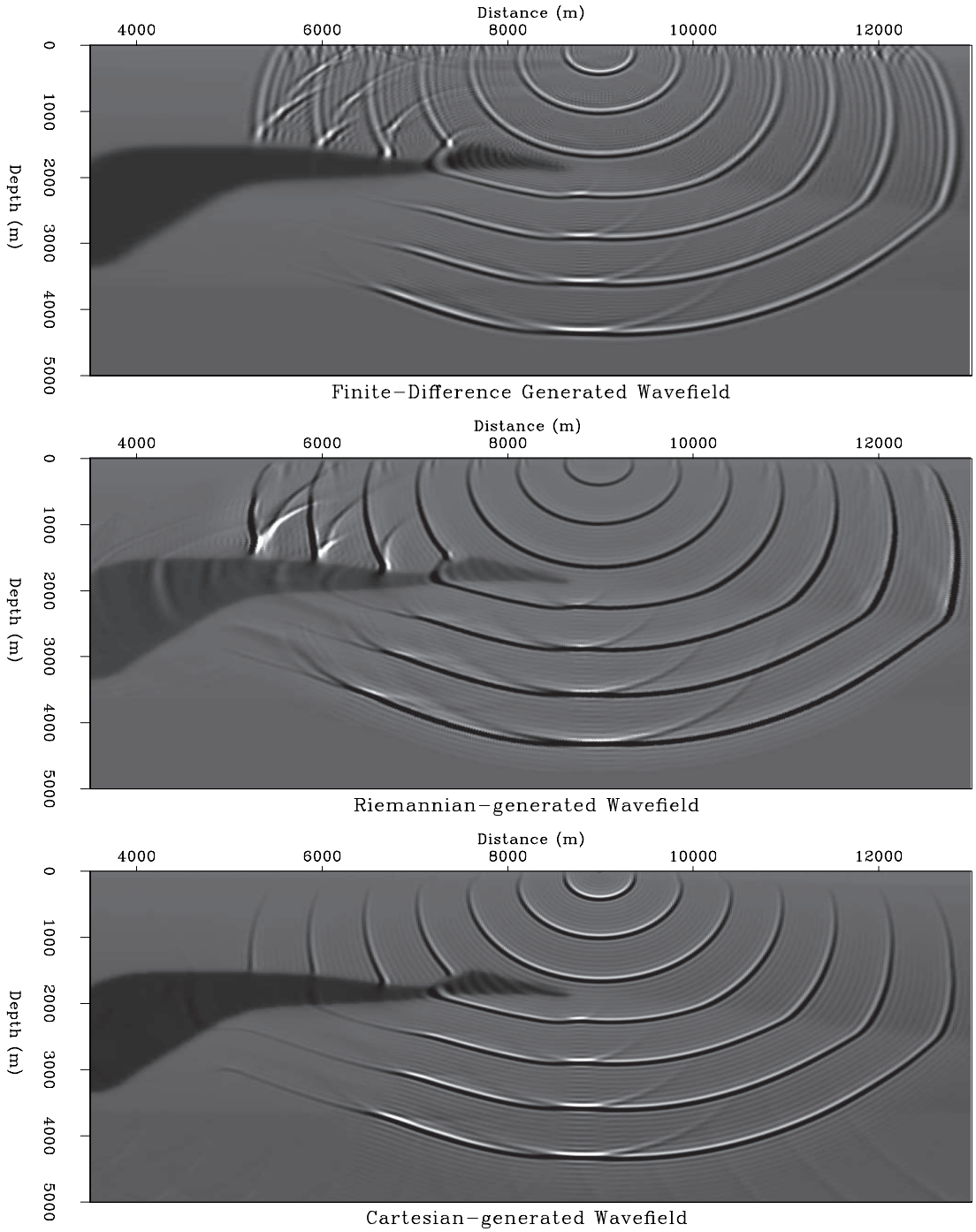
Distance (m)
4000
6000
8000
10000
12000
Depth (m)
0
1000
2000
3000
4000
5000
Finite−Difference Generated Wavefield
Distance (m)
4000
6000
8000
10000
12000
Depth (m)
0
1000
2000
3000
4000
5000
Riemannian−generated Wavefield
Distance (m)
4000
6000
8000
10000
12000
Depth (m)
0
1000
2000
3000
4000
5000
Cartesian−generated Wavefield

Figure 6.

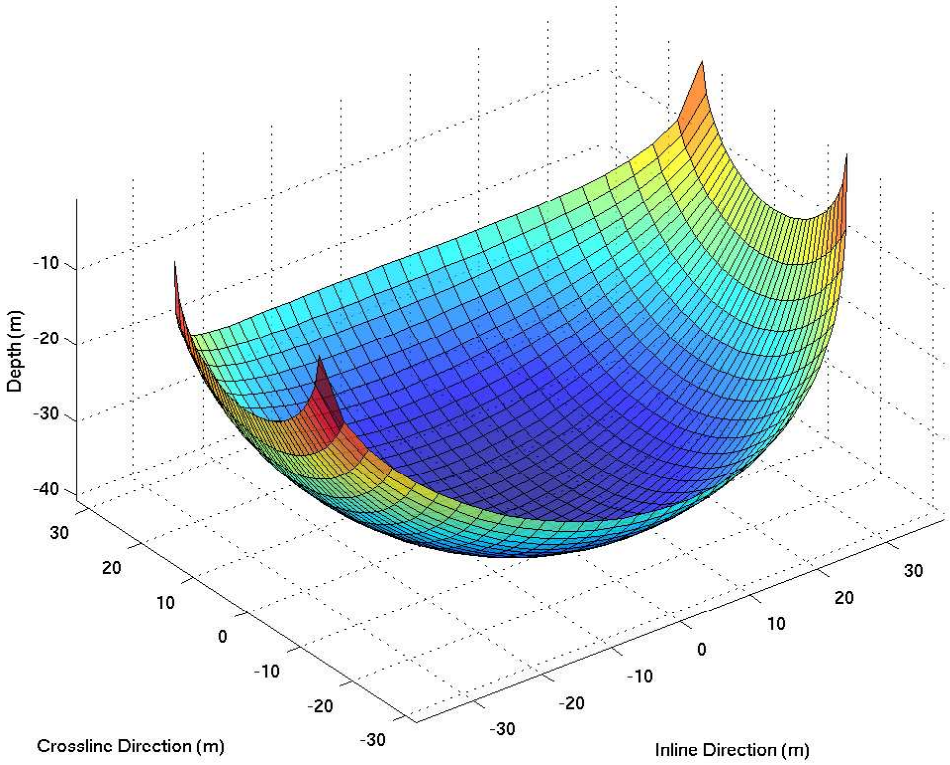
Depth (m)
-10
-20
-30
-40
30
20
10
0
-10
-20
-30
Crossline Direction (m)
30
20
10
0
-10
-20
-30
Inline Direction (m)

Figure 7.

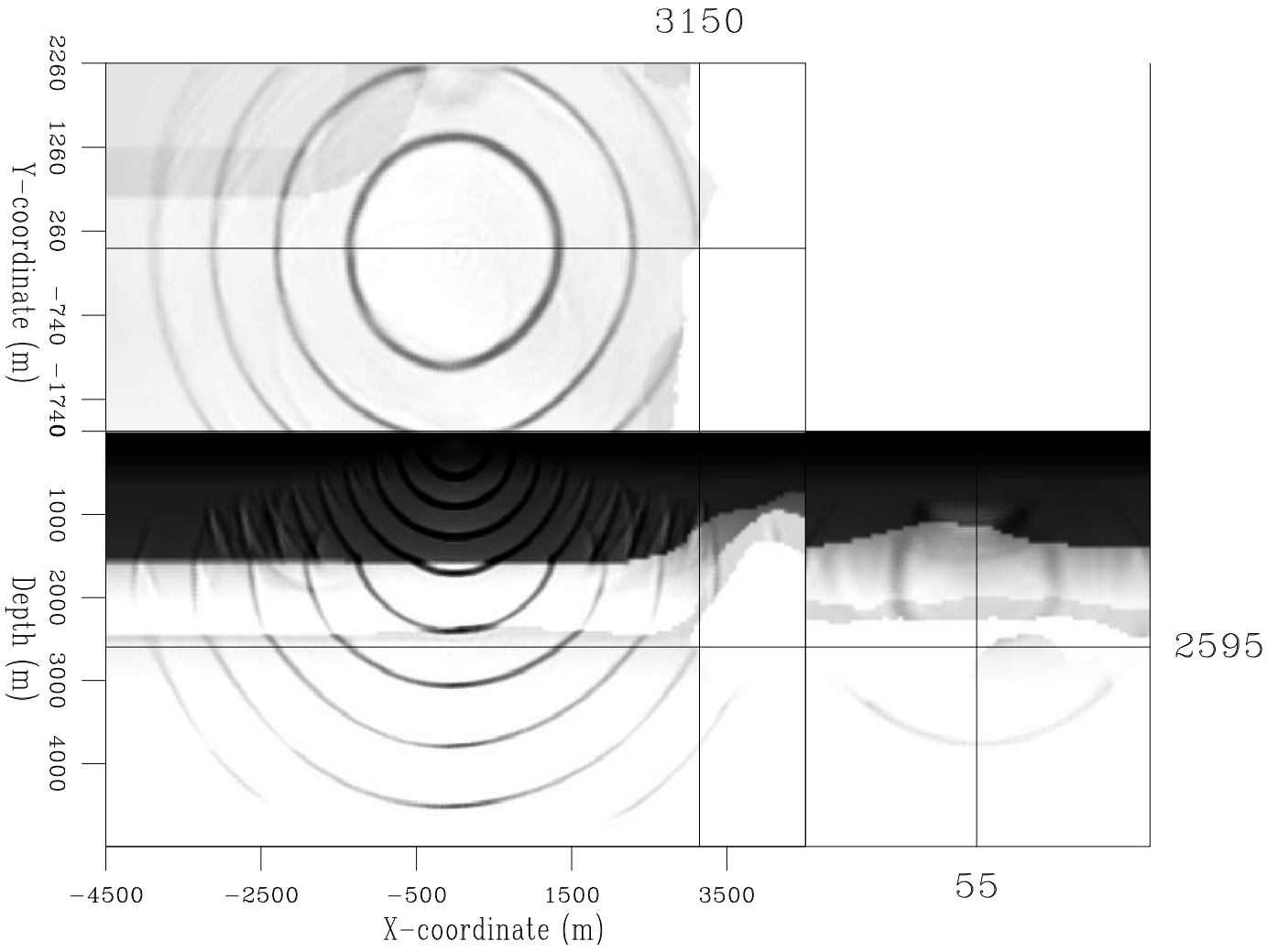
3150
2595
55
2260
1260
260
−740
−1740
1000
2000
3000
4000
Y−coordinate (m)
Depth (m)
−4500
−2500
−500
1500
3500
X−coordinate (m)

Figure 8.